

Accelerated Article Preview**Receptor binding and priming of the spike protein of SARS-CoV-2 for membrane fusion**

Received: 1 July 2020

Accepted: 11 September 2020

Accelerated Article Preview Published
online 17 September 2020

Cite this article as: Benton, D. J. et al. Receptor binding and priming of the spike protein of SARS-CoV-2 for membrane fusion. *Nature* <https://doi.org/10.1038/s41586-020-2772-0> (2020).

Donald J. Benton, Antoni G. Wrobel, Pengqi Xu, Chloë Roustan, Stephen R. Martin, Peter B. Rosenthal, John J. Skehel & Steven J. Gamblin

This is a PDF file of a peer-reviewed paper that has been accepted for publication. Although unedited, the content has been subjected to preliminary formatting. Nature is providing this early version of the typeset paper as a service to our authors and readers. The text and figures will undergo copyediting and a proof review before the paper is published in its final form. Please note that during the production process errors may be discovered which could affect the content, and all legal disclaimers apply.

Receptor binding and priming of the spike protein of SARS-CoV-2 for membrane fusion

<https://doi.org/10.1038/s41586-020-2772-0>

Received: 1 July 2020

Accepted: 11 September 2020

Published online: 17 September 2020

Donald J. Benton^{1,5}✉, Antoni G. Wrobel^{1,5}✉, Pengqi Xu^{4,1}, Chloë Roustan², Stephen R. Martin¹, Peter B. Rosenthal³, John J. Skehel¹ & Steven J. Gamblin¹✉

SARS-CoV-2 infection is initiated by virus binding to ACE2 cell surface receptors^{1–4}, followed by fusion of virus and cell membranes to release the virus genome into the cell. Both receptor binding and membrane fusion activities are mediated by the virus Spike glycoprotein, S^{5–7}. As with other class I membrane fusion proteins, S is post-translationally cleaved, in this case by furin, into S1 and S2 components that remain associated following cleavage^{8–10}. Fusion activation following receptor binding is proposed to involve the exposure of a second proteolytic site (S2'), cleavage of which is required for the fusion peptide release^{11,12}. We have investigated the binding of ACE2 to the furin-cleaved form of SARS-CoV-2 S by cryoEM. We classify ten different molecular species including the unbound, closed spike trimer, the fully open ACE2-bound trimer, and dissociated monomeric S1 bound to ACE2. The ten structures describe ACE2 binding events which destabilise the spike trimer, progressively opening up, and out, the individual S1 components. The opening process reduces S1 contacts and un-shields the trimeric S2 core, priming fusion activation and dissociation of ACE2-bound S1 monomers. The structures also reveal refolding of an S1 subdomain following ACE2 binding, that disrupts interactions with S2, notably involving Asp614^{13–15}, leading to destabilisation of the structure of S2 proximal to the secondary (S2') cleavage site.

Recognition of the ACE2 receptor by the Spike (S) membrane glycoprotein of SARS-CoV-2 is a major determinant of virus infectivity, pathogenesis, and host range. Previous structural studies on coronavirus S glycoproteins^{6,16–22} demonstrated that the S trimer consists of a central helical stalk, made of three interacting S2 components, which is covered at the top by S1. Each S1 component consists of two large domains, the N-terminal domain (NTD) and receptor-binding domain (RBD), each associated with a smaller intermediate subdomain. In virus membranes, Spike glycoproteins exist in a closed form, in which the RBDs cap the top of the S2 core and are inaccessible to ACE2, and in an open form, in which one S1 component has opened to expose the RBD for ACE2 binding^{6,16,18,23}. Recent structural studies on the isolated RBD of SARS-CoV-2 S in complex with ACE2^{7,24,25} provided a molecular description of the receptor-binding interface. Although some comparisons can be inferred from the previous cryoEM studies on the S of SARS-CoV^{12,18,19,23}, structures of intact trimeric SARS-CoV-2 S with bound ACE2 are needed to determine the effects of binding on overall Spike conformation.

To examine this interaction between the SARS-CoV-2 Spike and its receptor, we mixed ectodomains of furin-cleaved S with ectodomains of ACE2 and incubated them for ~60 s prior to plunge freezing in liquid ethane for examination by cryoEM. In the images obtained, we could resolve ten distinct species of S and S-ACE2 complexes (Fig. 1 & Extended Data Fig. 1), ranging from tightly-closed, unbound, trimers to open

trimers forming complexes with three ACE2 molecules and dissociated monomeric S1-ACE2 complexes. Of the S trimers analysed, 2/3 have an ACE2 bound (Extended Data Fig. 1). Of the unbound species, we observe good quality particles in the closed unbound conformation, equally compact to those reported in our previous study²⁶ and slightly more so than those described in earlier reports^{6,16}. There are also significant numbers (16% of all trimers) of unbound particles with one erect RBD, as well as some (4%) in an intermediate conformation, a less compact closed form, with a single disordered RBD, also reported in our previous study of furin-cleaved S²⁶.

Of the S trimers bound to receptor, half accommodate one ACE2 receptor. As reported previously for SARS-CoV S^{12,23} the ACE2-bound RBD occupies a range of tilts with respect to the long axis of the trimer (Extended Data Fig. 2A). Of the two RBDs per trimer that are not engaged with the receptor, either both are closed or one of the RBDs remains closed and one (either clockwise or anticlockwise to the bound S1 [Extended Data Fig. 1]) is in the open conformation. We were also able to identify, reconstruct, and refine trimers with two or three ACE2 receptors bound, in successively more open structures (Fig. 1 & Extended Data Fig. 1).

Two points emerge from comparing trimers with one erect RBD that is either bound or unbound by an ACE2 receptor. Firstly, ACE2 binding alters the position of the open RBD by a rigid-body rotation of the domain that moves its centre of mass on average a further ~5.5

¹Structural Biology of Disease Processes Laboratory, Francis Crick Institute, London, UK. ²Structural Biology Science Technology Platform, Francis Crick Institute, London, UK. ³Structural Biology of Cells and Viruses Laboratory, Francis Crick Institute, London, UK. ⁴Precision Medicine Center, The Seventh Affiliated Hospital, Sun Yat-sen University, Shenzhen, China. ⁵These authors contributed equally: Donald J. Benton, Antoni G. Wrobel. ✉e-mail: donald.benton@crick.ac.uk; antoni.wrobel@crick.ac.uk; steve.gamblin@crick.ac.uk

Å away from the trimer axis, the NTD-associated and RBD-associated subdomains of the same monomer shift -1.9 Å and -2.3 Å respectively (Extended Data Fig. 2C) and at the same time the NTDs of all three S1 components move by $-1.5 - 3.0$ Å (Extended Data Fig. 2D). Similar changes in the domain orientation are observed in the recent structure of the SARS-CoV-2 S complex with C105 Fab (Extended Data Fig. 2E)²⁷, which binds at the ACE2 binding site. However, the molecular basis of both of these sets of changes remain unclear. Binding of more than one ACE2 molecule does not induce significant further changes in the average positioning of the RBD (Extended Data Fig. 2E). Secondly, our data suggest that ACE2 binding favours the open conformation of RBD. The relatively high affinity interaction of RBD with ACE2, generates an RBD/ACE2 structure that cannot be accommodated in a closed trimer – the bound state does not have access to the closed conformation. Additionally, the fact that ACE2 binding induces a more open conformation of spike RBD implies that some of the binding energy is used to drive the new conformation of S1, which is then further excluded from a closed state.

The successive steps, from closed unbound trimer to the fully open, three-ACE2-bound trimer, are associated with a substantial reduction in the contact area each S1 makes with both its neighbouring S1 monomers and with the S2 trimeric core (Extended Data Table 1). For the fully, three-ACE2-bound species, each S1 makes 1400 Å² less contact with both its S1 trimer neighbours and 1300 Å² less contact with the S2 core than in the fully-closed trimer conformation; all these rearrangements being driven by the energetics of three ACE2 binding events. The movements of the RBD and NTD domains of S1 associated with the opening of the structure and stabilisation of the new arrangement by ACE2 binding, described above, leaves a trimeric ring of S1 molecules attached to the S2 core only through contacts with its two small intermediate subdomains (Fig. 2a). Comparing the ACE2-bound, open form (the open-unbound structure is similar but of poorer local resolution) with the fully-closed trimer, the RBD-associated intermediate subdomain moves about 8 Å, while the NTD-associated intermediate subdomain moves by 3 Å (Fig. 2a). The latter also undergoes a partial restructuring with possibly important implications for the mechanism of fusion activation of S. In the closed form, one edge of the NTD-associated intermediate subdomain interacts with a short helix and a loop from S2 of the neighbouring monomer (Fig. 2b). Two particularly noteworthy components of this interaction are a series of side chain π -stacking interactions in the closed structure²⁶: Tyr636, Phe318 and Arg634 of S1 with Tyr837 of S2; and a salt bridge formed by Asp614 of S1 with Lys854 of S2. In contrast, in the ACE2-bound form, Tyr636, Phe318, and Trp633 refold to the side of the domain further away from the symmetry axis (**as viewed in Fig. 2c**), leaving a channel to accommodate a new segment of a helix that forms downstream of Asp614 from polypeptide chain that was previously disordered. As a consequence, the interactions between S1 and S2 described above for the closed form are lost in the ACE2-bound form and the 827-855 segment of S2 becomes disordered (Fig. 2c). This part of S2 is immediately C-terminal to the putative fusion peptide of S2¹¹, the N-terminus of which is defined by Arg815 at the S2' cleavage site^{9,11}. ACE2-stabilised S1 opening therefore leads to destabilisation of S2 structure just after the putative fusion peptide, potentially activating it for exposure in the next stages of membrane fusion. It is noteworthy that Asp614, which salt bridges to S2 Lys854 in the closed form, is frequently substituted¹³⁻¹⁵ by a glycine residue and it has been suggested that this substitution reduces shedding of S1 (and increases the number of spikes on the virus surface)¹³. We also propose that this substitution would remove a key salt bridge, and that the unique stereochemistry available to glycine may facilitate the formation of the new segment of α -helix, which is also incompatible with the S2 interaction. Furthermore, it could lead to reduced stability of the closed form of S, which in turn would increase the likelihood of RBDs adopting the open conformation and hence the ability of S to bind to ACE2.

The opening up, and out, from the trimer axis, of the S1 domains with ACE2 binding gives rise to an un-shielding of the top surface of the helix-loop-helix (approximately residues 980-990 within the HRI region^{20,22,28,29}) at the top of the S2 domain (Fig. 3). In the closed form, these helices and their connecting turns are tightly shielded by the RBDs; each S2 monomer being predominantly covered by its anticlockwise related S1 trimer neighbour. In the fully open state, the S1 domains move in such a way as to generate a cavity of 50 Å diameter around the trimer axis that is about 65 Å deep. At the bottom of this cavity is the, now solvent exposed, central portion of HRI. For membrane fusion to occur, by comparison with other class I fusion proteins and as described in coronavirus post-fusion structures^{22,28,29}, the S2 component is likely to undergo a major helical rearrangement, in which the long trimer interface helix 1035:990 grows and extends, by incorporating the refolded turn and helix from the N-terminal portion of HRI, and projects the fusion peptide towards the host cell membrane. In this process, opening up of all three S1 monomers and their subsequent dissociation would enable the concerted helical refolding, since the cooperative displacement of the capping portions of the protein will likely be required for the extension of the helical coil, as recently observed for influenza haemagglutinin³⁰. The stoichiometry of S1 subunit:ACE2 interactions required for effective cell-surface contact or for priming is not addressed by our experiments. However, since the affinity of individual monomers for ACE2 appears to be sufficient for cellular association, it may be that more than one subunit is required to be in the open form for efficient priming of these rearrangements in S2 that occur in the process of membrane fusion. It seems reasonable to propose that the likelihood of triggering the fusion conformation increases with the number of ACE2 receptors bound.

In addition to the range of species of trimeric S described above, the largest single population of particles we were able to identify and reconstruct represent ACE2 bound to S1 monomer (Fig. 4). The interaction between ACE2 and the RBD, and the interaction of the latter with its associated intermediate subdomain, are very similar between the monomeric and trimer versions and with previously determined crystal and EM structures of RBD and ACE2^{7,24,25}. However, there are increasingly large rearrangements between the two intermediate subdomains and then with the NTD. By applying non-uniform refinement, the highest resolution was achieved for the reconstruction of the ACE2/RBD interaction, (Extended Data Fig. 4), in part because of the tight interaction but also likely because of the dominant influence of this part of the structure on the alignment process. Nevertheless, it is clear that there are both increasingly large changes in the interfaces between domains on moving towards the NTD and a range of sub-populations of related but, somewhat variable conformations. The high proportion of ACE2/S1 monomers, and the limited contact areas between the trimeric S1 ring interactions with S2, suggest that the fully open ACE2-bound spike complex is likely metastable.

Taken together, our structural data allow mechanistic suggestions for the early stages of SARS-CoV-2 infection of cells. SARS-CoV-2 S is produced in a compact closed form where the helices in the S2 membrane fusion component are capped by the RBD of neighbouring monomers. On cleavage by furin between the S1 and S2 domains, the proportion of the S trimers able to accommodate RBD in an open, ACE2-binding conformation increases²⁶. Binding of ACE2 receptor to open RBD leads to a more open trimer conformation. The geometry of ACE2 binding is incompatible with the RBD adopting a closed conformation and leads to our observation of several two-open-RBD conformations, and the three-RBD-bound conformation. Successive RBD openings and ACE2 binding lead to a fully open and ACE2-bound form where the trimeric S1 ring remains bound to the core S2 trimer by limited contacts through the intermediate subdomains of S1. This arrangement leaves the top of the S2 helices fully exposed. In the process, the interaction of the closed form of S1 with a segment of the S2 chain that precedes the putative fusion peptide region is lost in the open form. We suggest that in this

form the S trimer is primed for the helical rearrangements of S2 required for fusion of the viral and host cell membranes²⁸.

Online content

Any methods, additional references, Nature Research reporting summaries, source data, extended data, supplementary information, acknowledgements, peer review information; details of author contributions and competing interests; and statements of data and code availability are available at <https://doi.org/10.1038/s41586-020-2772-0>.

- Zhou, P. et al. A pneumonia outbreak associated with a new coronavirus of probable bat origin. *Nature* **579**, 270–273 (2020).
- Wan, Y., Shang, J., Graham, R., Baric, R. S. & Li, F. Receptor Recognition by the Novel Coronavirus from Wuhan: an Analysis Based on Decade-Long Structural Studies of SARS Coronavirus. *J. Virol.* (2020). <https://doi.org/10.1128/jvi.00127-20>.
- Li, F., Li, W., Farzan, M. & Harrison, S. C. Structural biology: Structure of SARS coronavirus spike receptor-binding domain complexed with receptor. *Science* (80-.). **309**, 1864–1868 (2005).
- Li, W. et al. Angiotensin-converting enzyme 2 is a functional receptor for the SARS coronavirus. *Nature* **426**, 450–454 (2003).
- Li, F. Structure, Function, and Evolution of Coronavirus Spike Proteins. *Annu. Rev. Virol.* (2016). <https://doi.org/10.1146/annurev-virology-110615-042301>.
- Walls, A. C. et al. Structure, Function, and Antigenicity of the SARS-CoV-2 Spike Glycoprotein. (2020). <https://doi.org/10.1016/j.cell.2020.02.058>.
- Shang, J. et al. Structural basis of receptor recognition by SARS-CoV-2. *Nature* 1–4 (2020). <https://doi.org/10.1038/s41586-020-2179-y>.
- Belouzard, S., Chu, V. C. & Whittaker, G. R. Activation of the SARS coronavirus spike protein via sequential proteolytic cleavage at two distinct sites. *Proc. Natl. Acad. Sci. U. S. A.* **106**, 5871–5876 (2009).
- Millet, J. K. & Whittaker, G. R. Host cell entry of Middle East respiratory syndrome coronavirus after two-step, furin-mediated activation of the spike protein. *Proc. Natl. Acad. Sci. U. S. A.* **111**, 15214–15219 (2014).
- Hoffmann, M. et al. SARS-CoV-2 Cell Entry Depends on ACE2 and TMPRSS2 and Is Blocked by a Clinically Proven Protease Inhibitor. *Cell* **181**, 271–280.e8 (2020).
- Lai, A. L., Millet, J. K., Daniel, S., Freed, J. H. & Whittaker, G. R. The SARS-CoV Fusion Peptide Forms an Extended Bipartite Fusion Platform that Perturbs Membrane Order in a Calcium-Dependent Manner. *J. Mol. Biol.* (2017). <https://doi.org/10.1016/j.jmb.2017.10.017>.
- Song, W., Gui, M., Wang, X. & Xiang, Y. Cryo-EM structure of the SARS coronavirus spike glycoprotein in complex with its host cell receptor ACE2. *PLoS Pathog.* (2018). <https://doi.org/10.1371/journal.ppat.1007236>.
- Zhang, L. et al. The D614G mutation in the SARS-CoV-2 spike protein reduces S1 shedding and increases infectivity. *bioRxiv* 2020.06.12.148726 (2020). <https://doi.org/10.1101/2020.06.12.148726>.
- Hu, J. et al. The D614G mutation of SARS-CoV-2 spike protein enhances viral infectivity 1 and decreases neutralization sensitivity to individual convalescent sera 2 Running Title: D614G mutant spike increases SARS-CoV-2 infectivity. *bioRxiv* (Cold Spring Harbor Laboratory, 2020). <https://doi.org/10.1101/2020.06.20.161323>.
- Korber, B. et al. Spike mutation pipeline reveals the emergence of a more transmissible form of SARS-CoV-2. *bioRxiv* 2020.04.29.069054 (2020). <https://doi.org/10.1101/2020.04.29.069054>.
- Wrapp, D. et al. Cryo-EM structure of the 2019-nCoV spike in the prefusion conformation. *Science* (80-.). (2020). <https://doi.org/10.1126/science.aax0902>.
- Alejandra Tortorici, M. et al. Structural basis for human coronavirus attachment to sialic acid receptors. *Nat. Struct. Mol. Biol.* (2019). <https://doi.org/10.1038/s41594-019-0233-y>.
- Yuan, Y. et al. Cryo-EM structures of MERS-CoV and SARS-CoV spike glycoproteins reveal the dynamic receptor binding domains. *Nat. Commun.* (2017). <https://doi.org/10.1038/ncomms15092>.
- Kirchdoerfer, R. N. et al. Stabilized coronavirus spikes are resistant to conformational changes induced by receptor recognition or proteolysis. *Sci. Rep.* (2018). <https://doi.org/10.1038/s41598-018-34171-7>.
- Pallesen, J. et al. Immunogenicity and structures of a rationally designed prefusion MERS-CoV spike antigen. *Proc. Natl. Acad. Sci. U. S. A.* **114**, E7348–E7357 (2017).
- Walls, A. C. et al. Cryo-electron microscopy structure of a coronavirus spike glycoprotein trimer. *Nature* (2016). <https://doi.org/10.1038/nature16988>.
- Cai, Y. et al. Distinct conformational states of SARS-CoV-2 spike protein. *Science* (80-.). eabd4251 (2020). <https://doi.org/10.1126/science.abd4251>.
- Gui, M. et al. Cryo-electron microscopy structures of the SARS-CoV spike glycoprotein reveal a prerequisite conformational state for receptor binding. *Cell Res.* (2017). <https://doi.org/10.1038/cr.2016.152>.
- Lan, J. et al. Structure of the SARS-CoV-2 spike receptor-binding domain bound to the ACE2 receptor. *Nature* **581**, 215–220 (2020).
- Yan, R. et al. Structural basis for the recognition of SARS-CoV-2 by full-length human ACE2. *Science* (80-.). **367**, 1444–1448 (2020).
- Wrobel, A. G. et al. SARS-CoV-2 and bat RaTG13 spike glycoprotein structures inform on virus evolution and furin-cleavage effects. *Nat. Struct. Mol. Biol.* 1–5 (2020). <https://doi.org/10.1038/s41594-020-0468-7>.
- Barnes, C. O. et al. Structures of Human Antibodies Bound to SARS-CoV-2 Spike Reveal Common Epitopes and Recurrent Features of Antibodies. *Cell* (2020). <https://doi.org/10.1016/j.cell.2020.06.025>.
- Walls, A. C. et al. Tectonic conformational changes of a coronavirus spike glycoprotein promote membrane fusion. *Proc. Natl. Acad. Sci. U. S. A.* (2017). <https://doi.org/10.1073/pnas.1708727114>.
- Fan, X., Cao, D., Kong, L. & Zhang, X. Cryo-EM analysis of the post-fusion structure of the SARS-CoV spike glycoprotein. *Nat. Commun.* **11**, 1–10 (2020).
- Benton, D. J., Gamblin, S. J., Rosenthal, P. B. & Skehel, J. J. Structural transitions in influenza haemagglutinin at membrane fusion pH. *Nature* **583**, 150–153 (2020).

Publisher's note Springer Nature remains neutral with regard to jurisdictional claims in published maps and institutional affiliations.

© The Author(s), under exclusive licence to Springer Nature Limited 2020

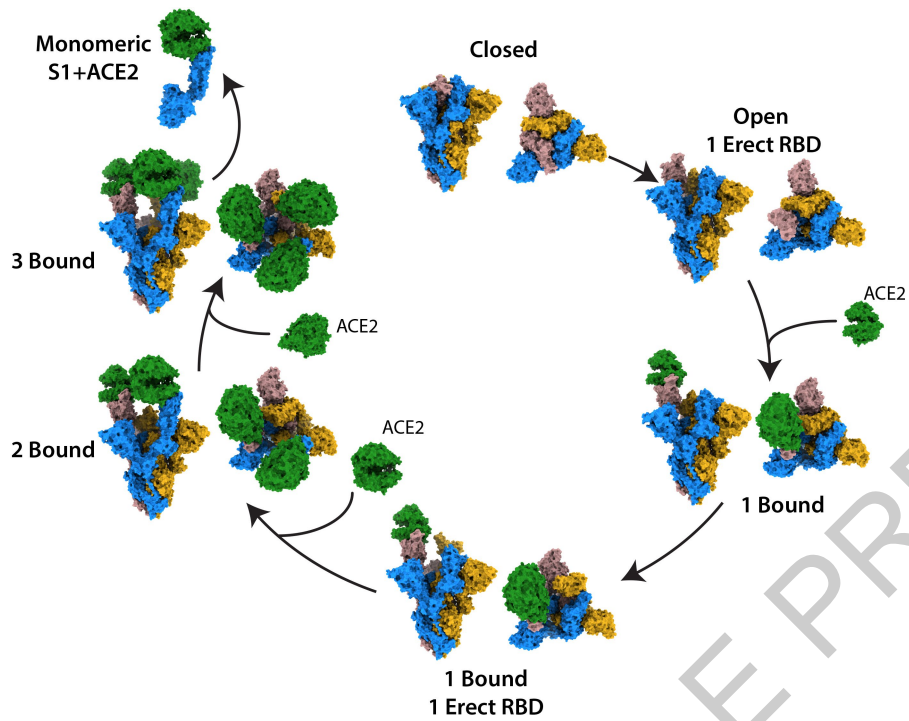


Fig. 1 | Sequential steps in ACE2 binding of SARS-CoV-2 S. Surface representation of S, with monomers coloured in blue, brown and gold, and ACE2 coloured in green. Each step shows two views of the S complexes with trimer axis vertical (left) and orthogonal top down view along the axis (right). Clockwise from top we show structures for closed, open but unbound RBD,

followed by sequential ACE2 binding events until we reach the fully-open, three-ACE2-bound S. From this final trimeric species we show dissociation into monomeric S1-ACE2, which may also occur for the one- or two-ACE2-bound species.

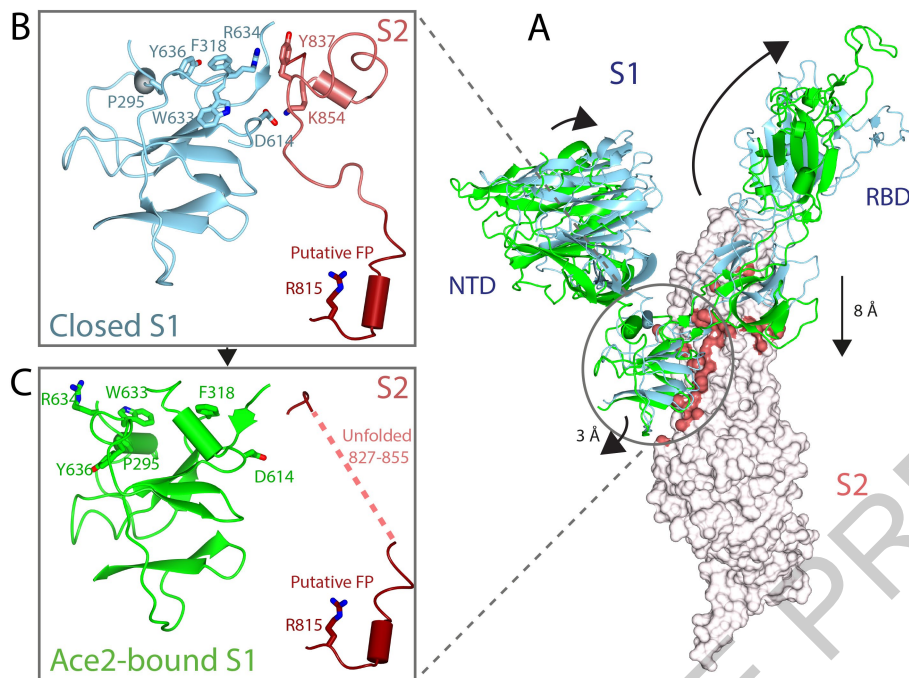


Fig. 2 | Structural rearrangements between the closed and the ACE2-bound states of S. (A) Surface representation of a monomer of S2 in one-ACE2-bound, two-RBD-closed state coloured in light pink with the S1 subunit of the adjacent monomer in ribbon representation: the S1 of one-ACE2-bound, two-RBD-closed state in green and the three-RBD-closed state (PDB 6ZGE²⁶) in blue. The atoms on the surface of S2 contacting the S1 intermediate domains are coloured in red. The arrows indicate the direction of movements of the intermediate domains, and of the RBD, between the closed and ACE2-bound conformations of S. (B) Ribbon representations of the NTD-associated intermediate domain in blue and the moiety of the S2 chain that it interacts

with, in red, in the closed conformation of S. Essential residues participating in the interaction are labelled with the salt bridge between Asp614 (S1, chain A) and Lys854 (S2, chain B) particularly of note. (C) Ribbon representation of the same intermediate domain as in (B) but in green in the conformation observed in the ACE2-bound structure of the spike, where the movement and refolding of the domain leads to a loss of interaction with S2, which becomes disordered. The putative Fusion Peptide (FP) and the S2' site of the second protease cleavage at R815 adjacent to the region that undergoes unfolding are shown in dark red.

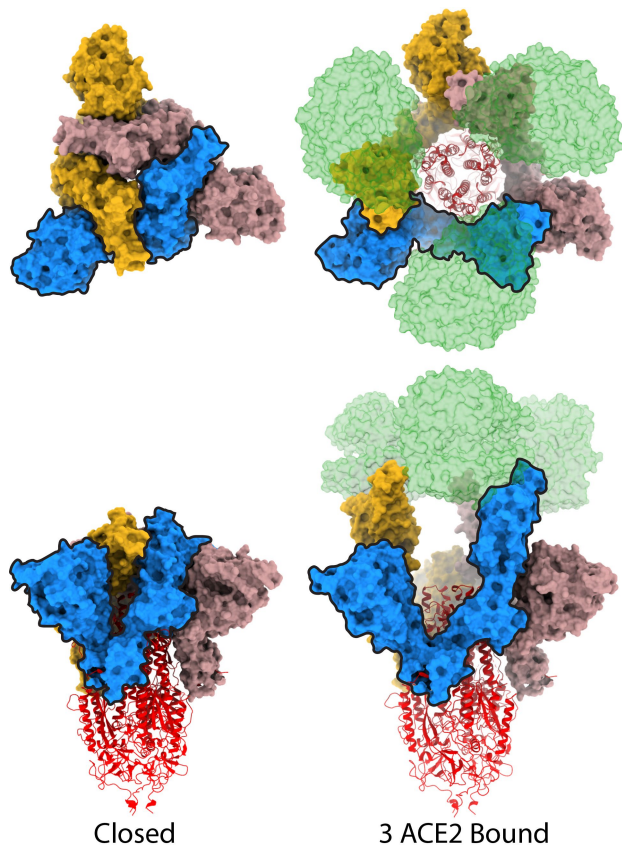
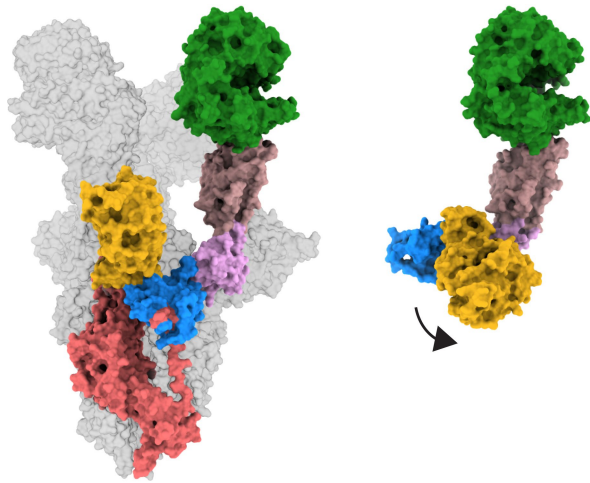


Fig. 3 | Structural basis of S2 unsheathing by ACE2 binding. S is shown as space filling representation for S1, with each monomer coloured blue, brown, and gold, and as a ribbons representation for S2 coloured in red for all three monomers. The left side shows a top down and side on view of the trimer in the closed conformation, while the right side shows the same views for the fully-open three-ACE2-bound species.



S1 + ACE2
Trimer

S1 + ACE2
Dissociated
Monomer

Fig. 4 | ACE2-bound S1 subunit as a part of the Strimer and as an isolated monomer. The right hand panel shows a space filling representation of S with one monomer coloured S1: NTD – yellow, NTD-associated subdomain 2 – blue, RBD-associated subdomain 2 – pink, RBD – brown, S2 – red, ACE2 – green; the rest of the trimer is coloured grey. The right-hand panel shows ACE2 bound to monomeric S1 in the same colours. The right hand panel is aligned on the RBD:ACE2 moiety of the trimer complex. The arrow indicates the direction of movement of the NTD and NTD-associated subdomain 2 on the transition from the trimer to the monomer species.

Methods

Constructs design, protein expression and purification

The ectodomains of ACE2 (19-615) and stabilised, '2P' mutant (K986P and V987P) of SARS-CoV-2 Spike (residues 1-1208) with intact furin cleavage site were prepared as described in our recent study²⁶. Briefly, the proteins were expressed in Expi293F cells (Gibco), harvested twice after 3-4 and 6-7 days, and purified with affinity chromatography (Spike using CoNTA resin from TAKARA, ACE2 with Streptactin XT resin from IBA Lifesciences), followed by gel filtration into a buffer containing 20 mM Tris pH 8.0 and 150 mM NaCl. As previously described, the purified Spike was then incubated for five hours with endogenous furin (New England Biolabs), after which the reaction was stopped by addition of EDTA.

EM sample preparation and data collection

R2/2 200 mesh Quantifoil grids were glow discharged for 30 s at 25 mA to prepare them for freezing. The furin-treated SARS-CoV-2 Spike was mixed with octyl glucoside as before²⁶ and, just 45-60 s before ultimately plunge freezing the grid, with concentrated ACE2 at 1 to 2 final molar ratio of trimeric spike to ACE2, aiming at the final concentration of spike at 0.5 mg/mL and octyl glucoside at 0.1%. 4 μ L of the obtained reaction mixture was then applied on a grid pre-equilibrated at 4 °C in 100% humidity, blotted with filter paper for 4-4.5 s using Vitrobot Mark III, and plunge frozen in liquid ethane.

Data were collected using EPU software on a Titan Krios microscope operating at 300 kV. Micrographs were collected using a Gatan K2 detector mounted on a Gatan GIF Quantum energy filter operating in zero-loss mode with a slit width of 20 eV. Exposures were 8 s, fractionated into 32 frames with an accumulated dose of 54.4 e⁻/Å², with a calibrated pixel size of 1.08 Å. Images were collected at a range of defoci between -1.5 and -3.0 μ m.

EM data processing

Movies were aligned using MotionCor2³¹ implemented in RELION³², followed by contrast transfer function (CTF) estimation using Ctfind4³³. Particles were picked using crYOLO³⁴ using a manually trained model. Particles were subjected to multiple rounds of 2D classification using cryoSPARC³⁵. Classes which displayed clear secondary structure were retained and split into subsets, which either resembled spike trimers or S1 monomers bound to ACE2. Initial models were made using the *ab initio* reconstruction in cryoSPARC. Different species containing trimeric S were separated by extensive 3D classification in RELION as shown on Extended Data Fig. 3. Prior to final refinements of particles corresponding to each of these species were subjected to Bayesian polishing in RELION³⁶ followed by homogeneous refinement in cryoSPARC coupled to CTF refinement. The monomeric S1-ACE2 complex was classified as in Extended Data Fig. 4A and refined using non-uniform-refinement in cryoSPARC coupled to CTF refinement. The final particles from the S1-ACE2 complex were subjected to an unmasked refinement in RELION to better resolve less ordered domains, with an overall lower global resolution (Extended Data Figs. 4B&C). Local resolution was estimated using blocres³⁷ implemented in cryoSPARC. Maps were locally filtered and globally sharpened³⁸ in cryoSPARC (Extended Data Figs. 5&6).

Model building

The model for the monomeric S1-ACE2 complex was based on the previously determined crystal structure (PDB: 6MOJ²⁴), with additional parts of the RBD and intermediate domain taken from our previous structure of the closed trimer 6ZGE²⁶. Models of the trimer structures were built using structures from our previous study²⁶ for the closed trimer (PDB: 6ZGE) and the one-erect-RBD structure (PDB: 6ZGG). The RBD-ACE2 parts of the model were built using the structure from the high resolution S1-ACE2 complex from this study. Models were manually adjusted

using COOT³⁹. The models of S1-ACE2 and the one-ACE2-bound closed structure were refined and validated using PHENIX real space refine⁴⁰. The other, lower resolution models were refined using NAMDINATOR⁴¹ and geometry minimization and validation in PHENIX. Measurements were made using Chimera⁴², CCP4MG⁴³, and PISA⁴⁴, with structures aligned on the large helix of S2 (residues 986-1032).

Reporting summary

Further information on research design is available in the Nature Research Reporting Summary linked to this paper.

Data availability

Maps and models have been deposited in the Electron Microscopy Data Bank, <http://www.ebi.ac.uk/pdbe/emdb/> and the Protein Data Bank, <https://www.ebi.ac.uk/pdbe/> with the following accession codes: EMD-11681 and PDB 7A91 (Dissociated S1 domain bound to ACE2 [Non-Uniform Refinement]); EMD-11682 and PDB 7A92 (Dissociated S1 domain bound to ACE2 [Unmasked Refinement]); EMD-11683 and PDB 7A93 (SARS-CoV-2 S with 2 RBDs Erect); EMD-11684 and PDB 7A94 (SARS-CoV-2 S with 1 ACE2 Bound); EMD-11685 and PDB 7A95 (SARS-CoV-2 S with 1 ACE2 Bound and 1 RBD Erect in Clockwise Direction); EMD-11686 and PDB 7A96 (SARS-CoV-2 S with 1 ACE2 Bound and 1 RBD Erect in Anticlockwise Direction); EMD-11687 and PDB 7A97 (SARS-CoV-2 S with 2 ACE2 Bound); EMD-11688 and PDB 7A98 (SARS-CoV-2 S with 3 ACE2 Bound).

- Zheng, S. Q. *et al.* MotionCor2: anisotropic correction of beam-induced motion for improved cryo-electron microscopy. *Nat. Methods* **14**, 331-332 (2017).
- Scheres, S. H. W. RELION: Implementation of a Bayesian approach to cryo-EM structure determination. *J. Struct. Biol.* **180**, 519-530 (2012).
- Rohou, A. & Grigorieff, N. CTFFIND4: Fast and accurate defocus estimation from electron micrographs. *J. Struct. Biol.* **192**, 216-221 (2015).
- Wagner, T. *et al.* SPHIRE-crYOLO is a fast and accurate fully automated particle picker for cryo-EM. *Commun. Biol.* **2**, (2019).
- Punjani, A., Rubinstein, J. L., Fleet, D. J. & Brubaker, M. A. cryoSPARC: algorithms for rapid unsupervised cryo-EM structure determination. *Nat. Methods* **14**, 290-296 (2017).
- Zivanov, J., Nakane, T. & Scheres, S. H. W. A Bayesian approach to beam-induced motion correction in cryo-EM single-particle analysis. *IUCr* **6**, 5-17 (2019).
- Cardone, G., Heymann, J. B. & Steven, A. C. One number does not fit all: Mapping local variations in resolution in cryo-EM reconstructions. *J. Struct. Biol.* (2013). <https://doi.org/10.1016/j.jsb.2013.08.002>.
- Rosenthal, P. B. & Henderson, R. Optimal Determination of Particle Orientation, Absolute Hand, and Contrast Loss in Single-particle Electron Cryomicroscopy. *J. Mol. Biol.* **333**, 721-745 (2003).
- Emsley, P., Lohkamp, B., Scott, W. G., Cowtan, K. & IUCr. Features and development of Coot. *Acta Crystallogr. Sect. D Biol. Crystallogr.* **66**, 486-501 (2010).
- Adams, P. D. *et al.* PHENIX: a comprehensive Python-based system for macromolecular structure solution. *Acta Crystallogr. Sect. D Biol. Crystallogr.* **66**, 213-221 (2010).
- Kidmose, R. T. *et al.* Namdinator - Automatic molecular dynamics flexible fitting of structural models into cryo-EM and crystallography experimental maps. *IUCr* **6**, 526-531 (2019).
- Pettersen, E. F. *et al.* UCSF Chimera - A visualization system for exploratory research and analysis. *J. Comput. Chem.* (2004). <https://doi.org/10.1002/jcc.20084>.
- McNicholas, S., Potterton, E., Wilson, K. S. & Noble, M. E. M. Presenting your structures: The CCP4mg molecular-graphics software. *Acta Crystallogr. Sect. D Biol. Crystallogr.* **67**, 386-394 (2011).
- Krissinel, E. & Henrick, K. Inference of Macromolecular Assemblies from Crystalline State. *J. Mol. Biol.* **372**, 774-797 (2007).

Acknowledgements We would like to acknowledge Andrea Nans of the Structural Biology Science Technology Platform for assistance with data collection, Phil Walker and Andrew Purkiss of the Structural Biology Science Technology Platform and the Scientific Computing Science Technology Platform for computational support. We thank Lesley Calder, Peter Cherepanov, George Kassiotis and Svend Kjaer for discussions. This work was funded by the Francis Crick Institute which receives its core funding from Cancer Research UK (FC001078 and FC001143), the UK Medical Research Council (FC001078 and FC001143), and the Wellcome Trust (FC001078 and FC001143). P.X. is also supported by the 100 Top Talents Program of Sun Yat-sen University, the Sanming Project of Medicine in Shenzhen (SZSM201911003) and the Shenzhen Science and Technology Innovation Committee (Grant No. JCYJ20190809151611269).

Author contributions D.J.B, A.G.W, P.X, C.R, S.R.M performed research, collected and analysed data; D.J.B, A.G.W, P.B.R, J.J.S, S.J.G conceived and designed research and wrote the paper.

Competing interests The authors declare no competing interests.

Additional information

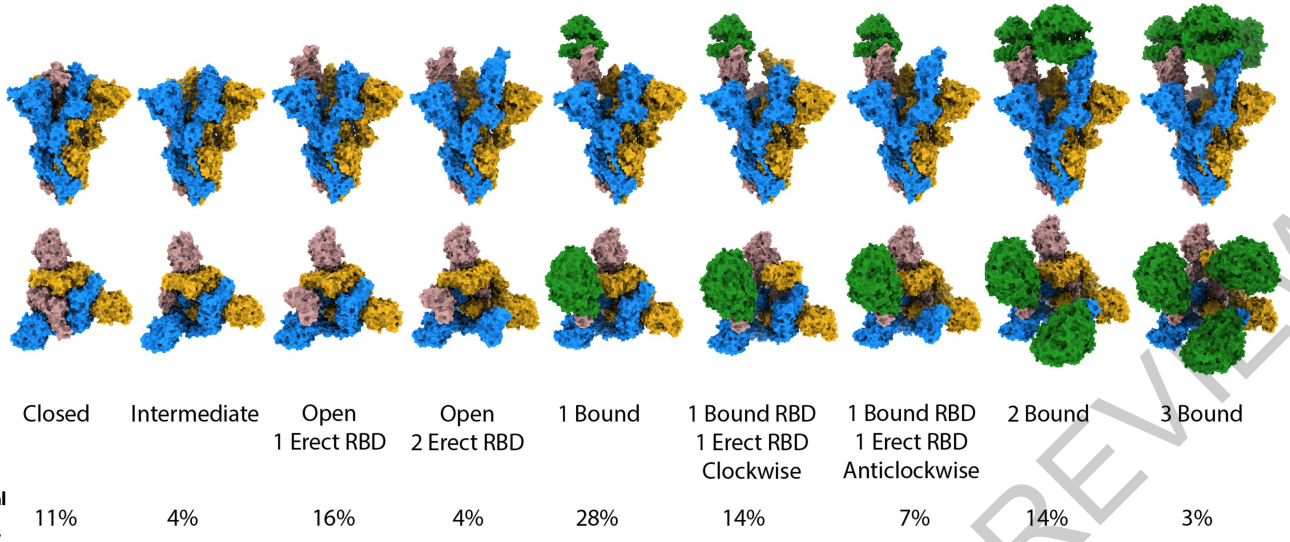
Supplementary information is available for this paper at <https://doi.org/10.1038/s41586-020-2772-0>.

Correspondence and requests for materials should be addressed to D.J.B., A.G.W. or S.J.G.

Peer review information *Nature* thanks Stephen Harrison and the other, anonymous, reviewer(s) for their contribution to the peer review of this work.

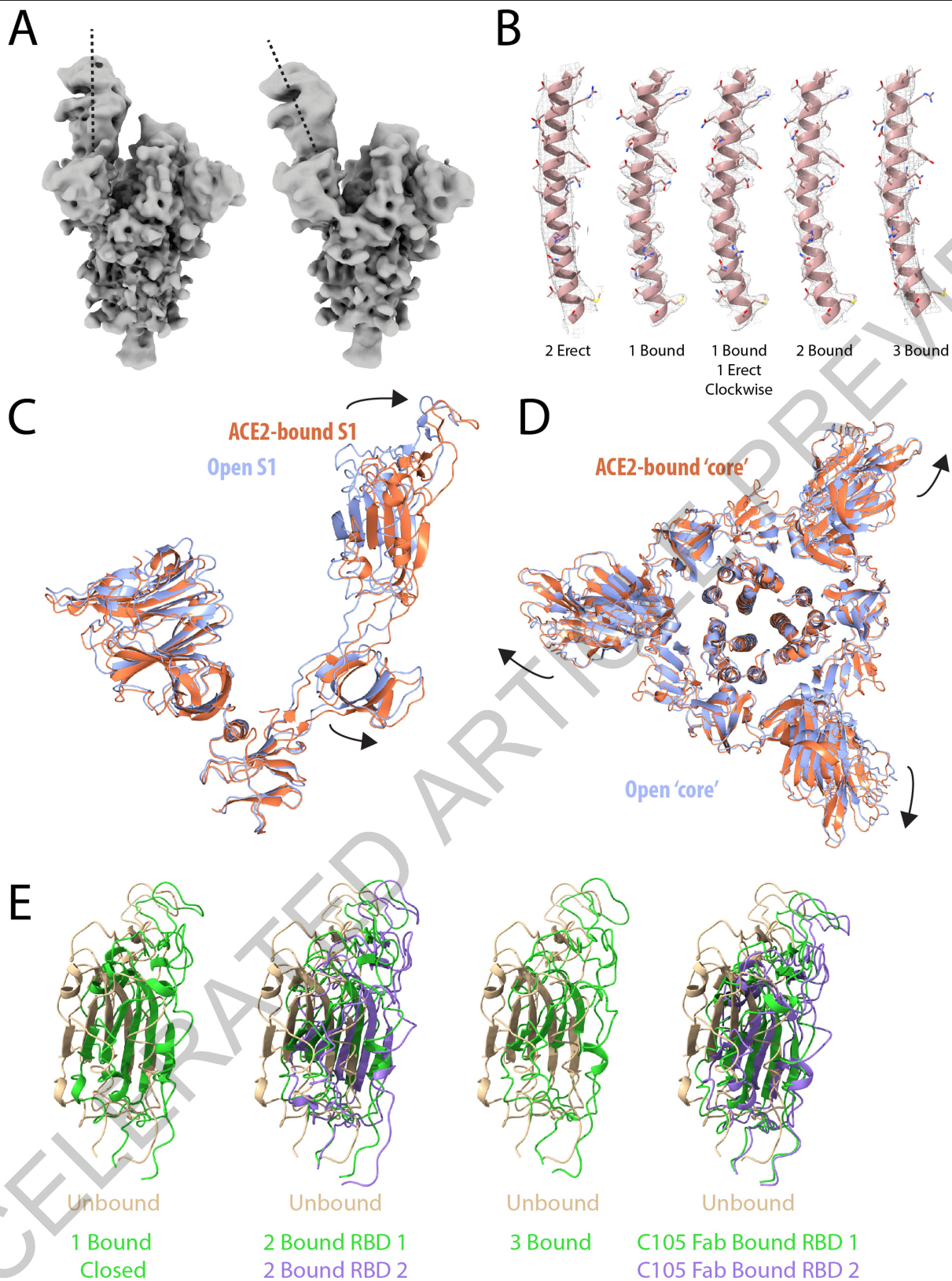
Reprints and permissions information is available at <http://www.nature.com/reprints>.

ACCELERATED ARTICLE PREVIEW



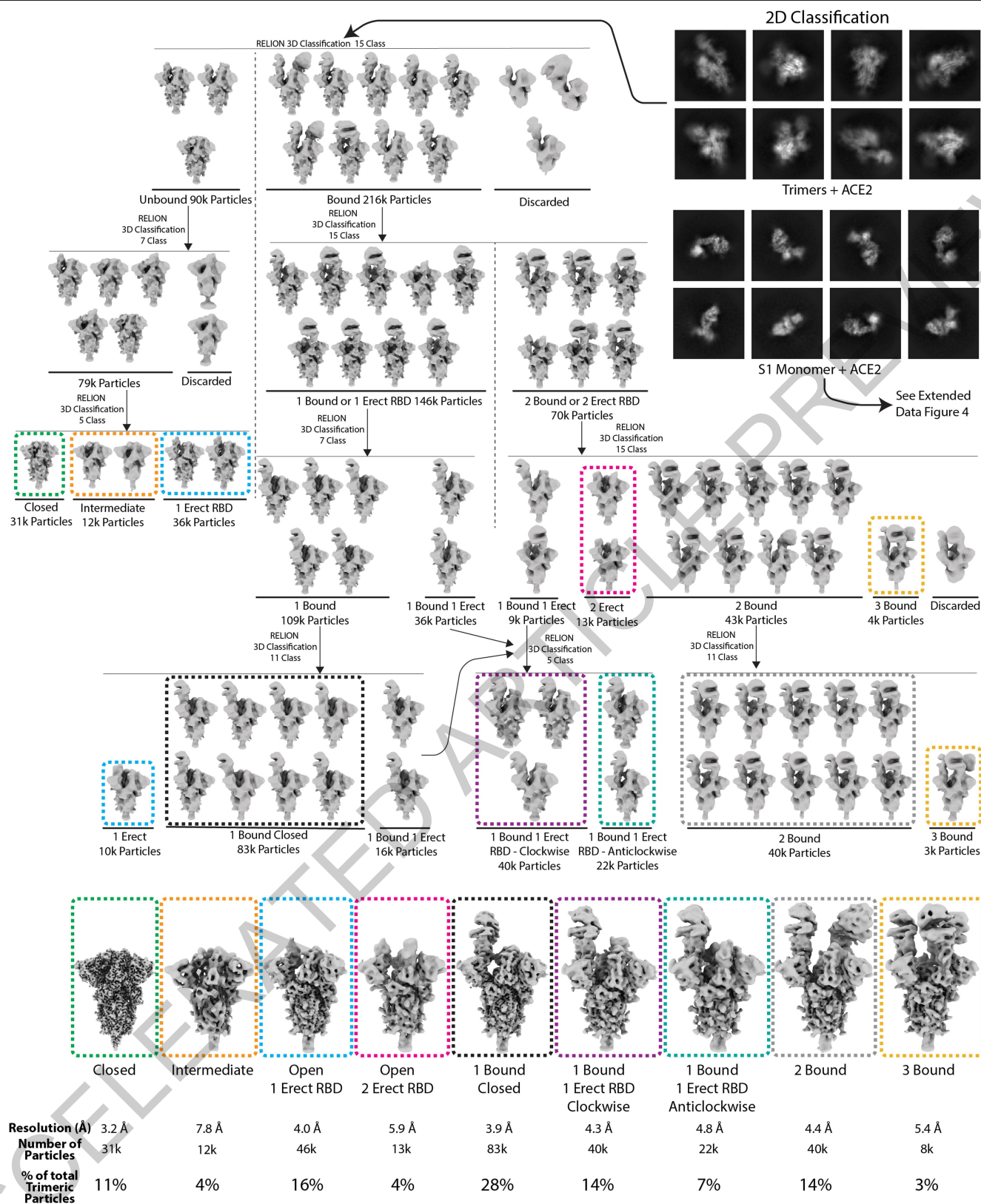
Extended Data Fig. 1 | Surface representation of obtained structures. The three monomers of S in each trimer are coloured in blue, pink and yellow with ACE2 shown in green. Relative percentages of all trimeric S particles used to calculate EM maps shown.

ACCELERATED ARTICLE PREVIEW



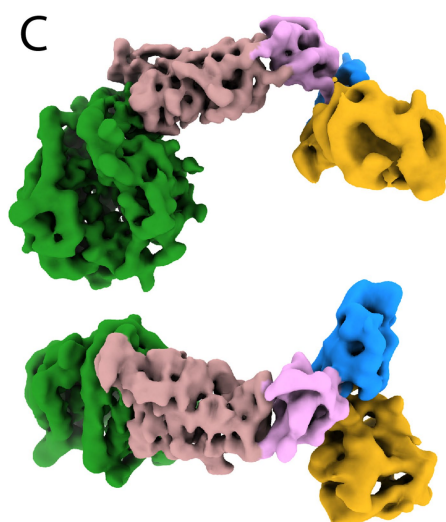
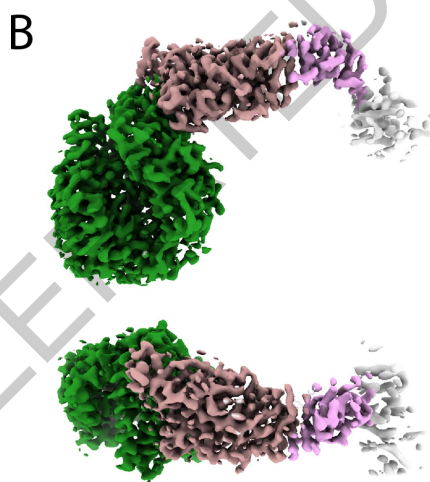
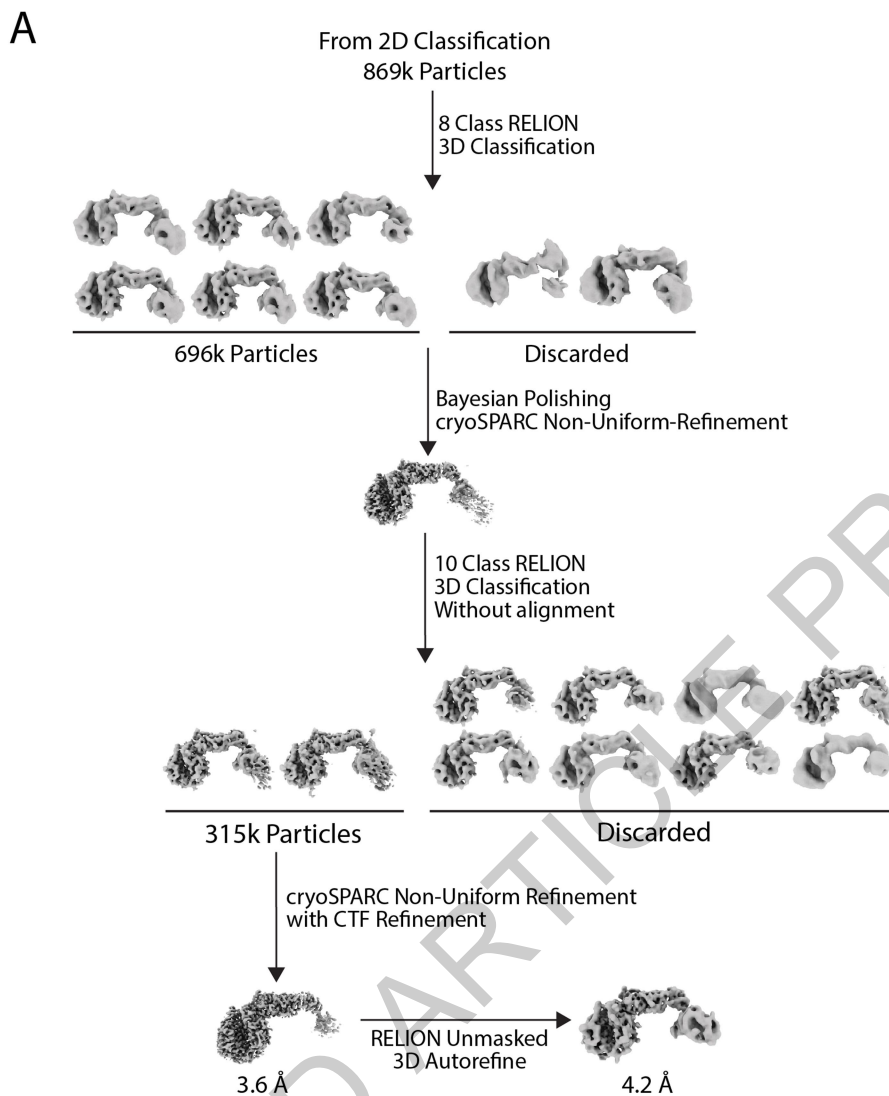
Extended Data Fig. 2 | Features of the Spike structures obtained. A) Two 3D classes, obtained by further classification of the one-Ace2-bound closed state from figure 1, representative of the range of motion of the RBD with bound ACE2, tilting away from the trimer axis of the spike trimer. The tilt of the RBD and ACE2 is indicated with a dashed line. B) Representative density of different obtained EM maps for residues 996-1030 of S2. Built model shown in pink, with EM density shown as a mesh. C+D) Comparison of S structures for the open 1

erect RBD structure (purple) with the 1ACE2 bound structure (orange). C) S1 domains shown to highlight domain shifts of the RBD and RBD associated intermediate domain. D) Outwards movements of S domains (excluding RBDs). E) Comparison of RBD displacements of 1 Bound, 2 Bound and 3 Bound RBDs upon binding of ACE2 to the unbound open structure of S (beige). These are compared to the RBD displacement upon binding of the C105 Fab fragment²⁷, which binds at the ACE2 interface of the RBD (PDB: 6XCM).



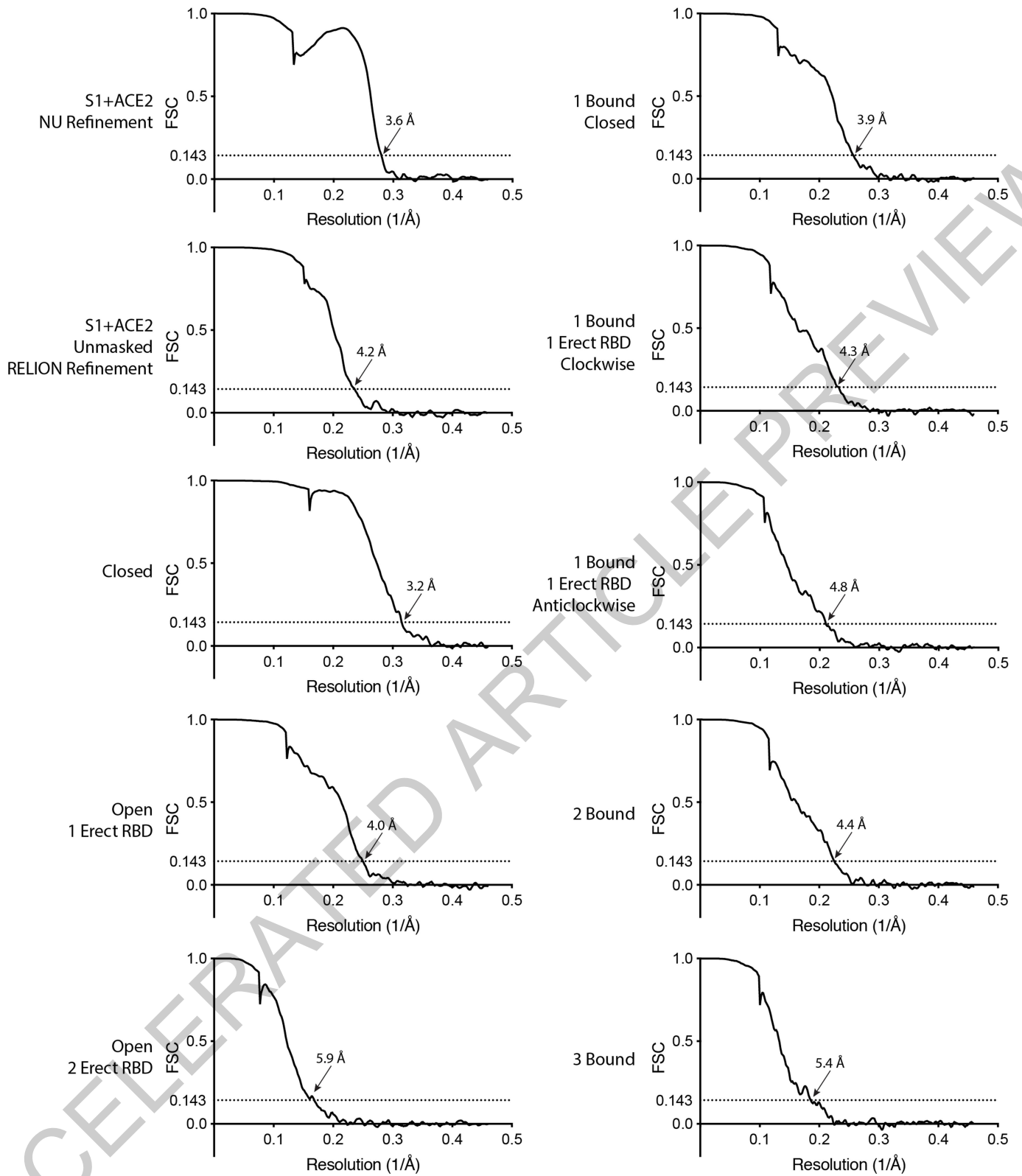
Extended Data Fig. 3 | Cryo-EM data processing scheme. Classes of particles used to obtain final Spike trimer structures, unbound and in complex with ACE2, are surrounded by a box of the same colour as the final maps shown at the

bottom. The global resolution, final particle number and percentage for each trimer species are shown at the bottom.

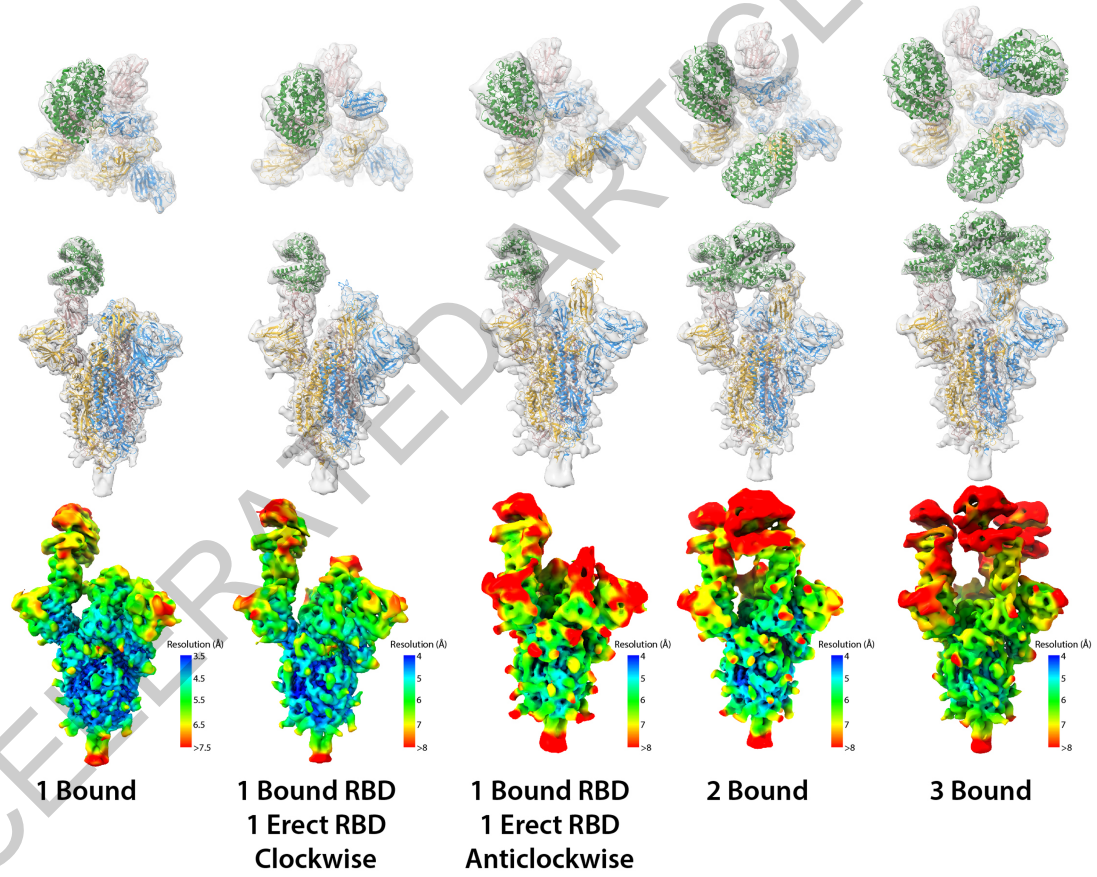
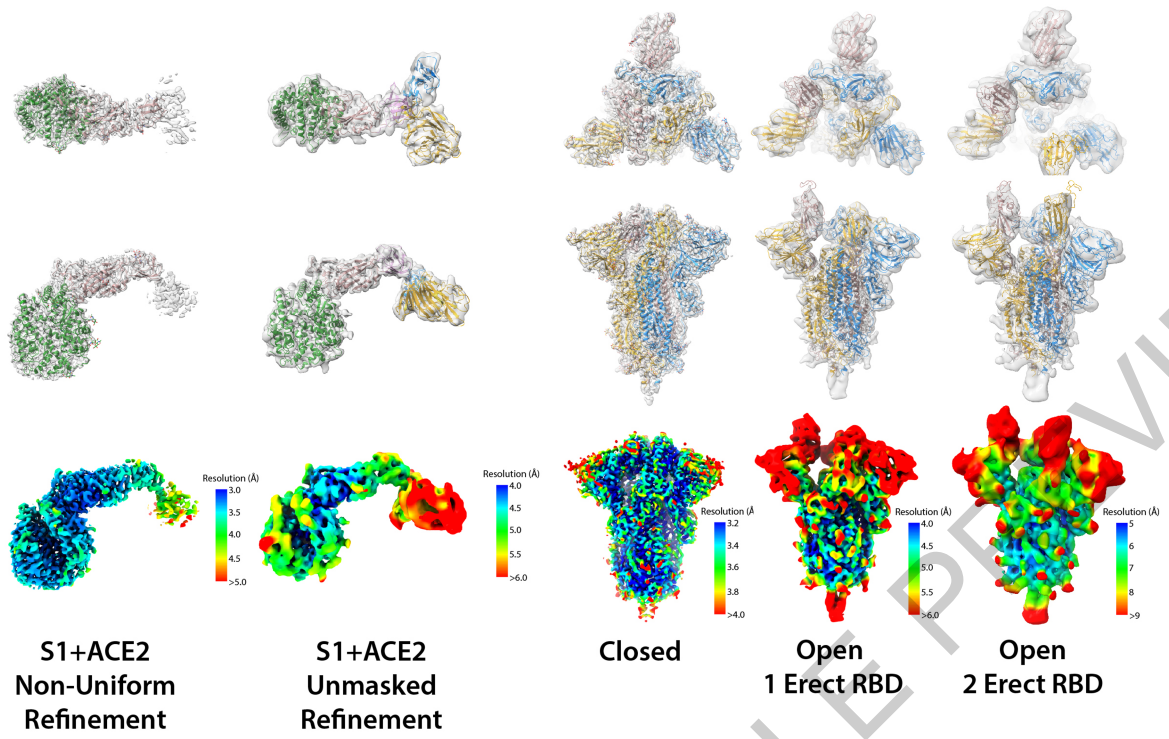


Extended Data Fig. 4 | Monomeric S1 bound to ACE2. A) Classification scheme for S1-ACE2 complex. Maps are shown of orthogonal views of the non-uniform refinement (B) and unmasked refinement (C) of the final particles.

Domains are coloured: ACE2 – green; NTD – yellow; RBD – rosy brown; RBD ganymede – pink; NTD ganymede – blue; disseminated S1 density in B) shown in cream.



Extended Data Fig. 5 | Fourier shell correlation (FSC) graphs for each of the determined structures.



Extended Data Fig. 6 | Maps and models of determined structures. Orthogonal views of EM density (grey) and ribbon diagram representation of the models built shown above, with EM maps coloured by local resolution shown below.

Article

Extended Data Table 1 | Buried interface surface area between monomers in different conformations of unbound and ACE2-bound trimers.

	Interface A to B (\AA^2)	Interface A to C (\AA^2)	Interface B to C (\AA^2)
UNBOUND			
Closed	5900	5900	5900
Open	4000	4500	4700
RECEPTOR BOUND			
1ACE2-bound, closed	3800	4200	4100
1ACE2-bound, open	3900	3900	4200
2ACE2-bound	3900	3900	4200
3ACE2-bound	3900	3900	3900

Interface area was calculated using PISA. In the open and ACE2-bound conformations, chain A is the one to open first and to bind the receptor first, then B follows, if second RBD changes the conformation. Chain B is the one counter-clockwise to A when looking down the symmetry axis with the membrane-proximal part at the bottom. The unbound and three-ACE2-bound molecules are of C3 symmetry.

Extended Data Table 2 | Cryo-EM data collection, refinement and validation statistics.

	S1+ACE2 Non-uniform Refinement (EMDB-11681) (PDB 7A91)	S1+ACE2 Unmasked Refinement (EMDB-11682) (PDB 7A92)	2 Erect RBD (EMDB-11683) (PDB 7A93)	1 ACE2 Bound Closed (EMDB-11684) (PDB 7A94)	1 ACE2 Bound 1 Erect RBD Clockwise (EMDB-11685) (PDB 7A95)	1 ACE2 Bound 1 Erect RBD Anticlockwise (EMDB-11686) (PDB 7A96)	2 ACE2 Bound (EMDB-11687) (PDB 7A97)	3ACE2 Bound (EMDB-11688) (PDB 7A98)
Data collection and processing								
Voltage (kV)	300	300	300	300	300	300	300	300
Electron exposure (e-/Å ²)	54.4	54.4	54.4	54.4	54.4	54.4	54.4	54.4
Defocus range (µm)	-1.5 to -3.0	-1.5 to -3.0	-1.5 to -3.0	-1.5 to -3.0	-1.5 to -3.0	-1.5 to -3.0	-1.5 to -3.0	-1.5 to -3.0
Pixel size (Å)	1.08	1.08	1.08	1.08	1.08	1.08	1.08	1.08
Symmetry imposed	C1	C1	C1	C1	C1	C1	C1	C3
Final particle images (no.)	315 k	315 k	13 k	83 k	40 k	22 k	40 k	8 k
Map resolution (Å)	3.6	4.2	5.9	3.9	4.3	4.8	4.4	5.4
FSC threshold = 0.143								
Map resolution range (Å)	3 - 5	4 - 6	5 - 9	3.5 - 7.5	4 - 8	4 - 8	4 - 8	5 - 8
Refinement								
Initial model used (PDB code)	6MOJ	-	-	-	-	-	-	-
Model resolution (Å)	3.6	4.4	6.7	4.0	4.4	4.9	4.6	6.1
FSC threshold = 0.5								
Map sharpening <i>B</i> factor (Å ²)	-98.4	-158.9	-169.6	-75.0	-64.7	-66.1	-67.2	-119.6
Model composition								
Non-hydrogen atoms	6915	10040	25243	30475	29904	29828	34645	39456
Protein residues	839	1231	3221	3825	3794	3783	4373	4962
Ligands	10	10	-	24	-	-	-	-
R.m.s. deviations								
Bond lengths (Å)	0.006	0.007	0.004	0.007	0.004	0.004	0.004	0.004
Bond angles (°)	0.763	1.151	0.889	0.859	0.906	0.906	0.899	0.918
Validation								
MolProbity score	1.46	1.55	1.62	1.57	1.71	1.75	1.81	1.85
Clashscore	3.25	3.71	2.83	3.38	3.48	3.88	4.85	5.71
Poor rotamers (%)	0.81	1.10	0.85	0.90	0.90	0.82	0.23	0.83
Ramachandran plot								
Favored (%)	95.07	94.81	90.11	93.16	88.97	89.21	89.70	90.23
Allowed (%)	4.93	5.02	9.89	6.84	11.03	10.77	10.28	9.65
Disallowed (%)	0.00	0.16	0.00	0.00	0.00	0.03	0.02	0.12

Reporting Summary

Nature Research wishes to improve the reproducibility of the work that we publish. This form provides structure for consistency and transparency in reporting. For further information on Nature Research policies, see [Authors & Referees](#) and the [Editorial Policy Checklist](#).

Statistics

For all statistical analyses, confirm that the following items are present in the figure legend, table legend, main text, or Methods section.

- | n/a | Confirmed |
|-------------------------------------|---|
| <input checked="" type="checkbox"/> | <input type="checkbox"/> The exact sample size (n) for each experimental group/condition, given as a discrete number and unit of measurement |
| <input checked="" type="checkbox"/> | <input type="checkbox"/> A statement on whether measurements were taken from distinct samples or whether the same sample was measured repeatedly |
| <input checked="" type="checkbox"/> | <input type="checkbox"/> The statistical test(s) used AND whether they are one- or two-sided
<i>Only common tests should be described solely by name; describe more complex techniques in the Methods section.</i> |
| <input checked="" type="checkbox"/> | <input type="checkbox"/> A description of all covariates tested |
| <input checked="" type="checkbox"/> | <input type="checkbox"/> A description of any assumptions or corrections, such as tests of normality and adjustment for multiple comparisons |
| <input checked="" type="checkbox"/> | <input type="checkbox"/> A full description of the statistical parameters including central tendency (e.g. means) or other basic estimates (e.g. regression coefficient) AND variation (e.g. standard deviation) or associated estimates of uncertainty (e.g. confidence intervals) |
| <input checked="" type="checkbox"/> | <input type="checkbox"/> For null hypothesis testing, the test statistic (e.g. F , t , r) with confidence intervals, effect sizes, degrees of freedom and P value noted
<i>Give P values as exact values whenever suitable.</i> |
| <input checked="" type="checkbox"/> | <input type="checkbox"/> For Bayesian analysis, information on the choice of priors and Markov chain Monte Carlo settings |
| <input checked="" type="checkbox"/> | <input type="checkbox"/> For hierarchical and complex designs, identification of the appropriate level for tests and full reporting of outcomes |
| <input checked="" type="checkbox"/> | <input type="checkbox"/> Estimates of effect sizes (e.g. Cohen's d , Pearson's r), indicating how they were calculated |

Our web collection on [statistics for biologists](#) contains articles on many of the points above.

Software and code

Policy information about [availability of computer code](#)

Data collection

Data analysis

For manuscripts utilizing custom algorithms or software that are central to the research but not yet described in published literature, software must be made available to editors/reviewers. We strongly encourage code deposition in a community repository (e.g. GitHub). See the Nature Research [guidelines for submitting code & software](#) for further information.

Data

Policy information about [availability of data](#)

All manuscripts must include a [data availability statement](#). This statement should provide the following information, where applicable:

- Accession codes, unique identifiers, or web links for publicly available datasets
- A list of figures that have associated raw data
- A description of any restrictions on data availability

Maps and models have been deposited in the Electron Microscopy Data Bank, <http://www.ebi.ac.uk/pdbe/emdb/> and the Protein Data Bank, <https://www.ebi.ac.uk/pdbe/> with the following accession codes: EMD-11681 and PDB 7A91 (Dissociated S1 domain bound to ACE2 [Non-Uniform Refinement]); EMD-11682 and PDB 7A92 (Dissociated S1 domain bound to ACE2 [Unmasked Refinement]); EMD-11683 and PDB 7A93 (SARS-CoV-2 S with 2 RBDs Erect); EMD-11684 and PDB 7A94 (SARS-CoV-2 S with 1 ACE2 Bound); EMD-11685 and PDB 7A95 (SARS-CoV-2 S with 1 ACE2 Bound and 1 RBD Erect in Clockwise Direction); EMD-11686 and PDB 7A96 (SARS-CoV-2 S with 1 ACE2 Bound and 1 RBD Erect in Anticlockwise Direction); EMD-11687 and PDB 7A97 (SARS-CoV-2 S with 2 ACE2 Bound); EMD-11688 and PDB 7A98 (SARS-CoV-2 S with 3 ACE2 Bound).

Field-specific reporting

Please select the one below that is the best fit for your research. If you are not sure, read the appropriate sections before making your selection.

Life sciences Behavioural & social sciences Ecological, evolutionary & environmental sciences

For a reference copy of the document with all sections, see [nature.com/documents/nr-reporting-summary-flat.pdf](https://www.nature.com/documents/nr-reporting-summary-flat.pdf)

Life sciences study design

All studies must disclose on these points even when the disclosure is negative.

Sample size	All cryoEM datasets consist of several thousand images. The number of images were sufficient to achieve the reported resolution, according to the most commonly reported resolution measure in cryoEM described in Rosenthal and Henderson 2003, as cited in the manuscript
Data exclusions	CryoEM single particles were included and excluded within the image processing workflow using standard image processing techniques such as 2D and 3D classifications, as detailed in Extended Data Figures 3 and 4.
Replication	Structures were determined using independent half datasets, according to standard procedures in cryoEM. Images were collected from three independent replicate prepared grids, which all produced similar images both by low resolution visual inspection and high resolution class averages. There were no unsuccessful replications.
Randomization	Not applicable to this study, as samples were not assigned to experimental groups and data were collected and processed according to standard techniques for cryoEM.
Blinding	Not applicable to this study, as there was no experimental group allocation in data collection and analysis.

Reporting for specific materials, systems and methods

We require information from authors about some types of materials, experimental systems and methods used in many studies. Here, indicate whether each material, system or method listed is relevant to your study. If you are not sure if a list item applies to your research, read the appropriate section before selecting a response.

Materials & experimental systems

n/a	Involvement in the study
<input checked="" type="checkbox"/>	<input type="checkbox"/> Antibodies
<input type="checkbox"/>	<input checked="" type="checkbox"/> Eukaryotic cell lines
<input checked="" type="checkbox"/>	<input type="checkbox"/> Palaeontology
<input checked="" type="checkbox"/>	<input type="checkbox"/> Animals and other organisms
<input checked="" type="checkbox"/>	<input type="checkbox"/> Human research participants
<input checked="" type="checkbox"/>	<input type="checkbox"/> Clinical data

Methods

n/a	Involvement in the study
<input checked="" type="checkbox"/>	<input type="checkbox"/> ChIP-seq
<input checked="" type="checkbox"/>	<input type="checkbox"/> Flow cytometry
<input checked="" type="checkbox"/>	<input type="checkbox"/> MRI-based neuroimaging

Eukaryotic cell lines

Policy information about [cell lines](#)

Cell line source(s)	expi293F cells were purchased from Thermo Scientific and used for protein expression
Authentication	Cell line used was not authenticated
Mycoplasma contamination	Cell line was not tested for mycoplasma contamination
Commonly misidentified lines (See ICLAC register)	Name any commonly misidentified cell lines used in the study and provide a rationale for their use.